Excitation-and-collection geometry insensitive fluorescence imaging of tissue-simulating turbid media

Jianan Y. Qu, Zhijian Huang, and Jianwen Hua

We present an imaging technique for the correction of geometrical effects in fluorescence measurement of optically thick, turbid media such as human tissue. Specifically, we use the cross-polarization method to reject specular reflection and enhance the diffusive backscattering of polarized fluorescence excitation light from the turbid media. We correct the nonuniformity of the image field caused by the excitation-and-collection geometry of a fluorescence imaging system by normalizing the fluorescence image to the cross-polarized reflection image. The ratio image provides a map of relative fluorescence yield, defined as the ratio of emerging fluorescence power to incident excitation, over the surface of an imaged homogeneous turbid medium when fluorescence excitation-and-collection geometries vary in a wide range. We investigate the mechanism of ratio imaging by using Monte Carlo modeling. Our findings show that this technique could have a potential use in the detection of early cancer, which usually starts from a superficial layer of tissue, based on the contrast in the tissue fluorescence of an early lesion and of the surrounding normal tissue.

OCIS codes: 170.0170, 110.7050, 170.3880, 170.4580, 170.6510.

1. Introduction

The light-induced fluorescence (LIF) imaging technique has been extensively investigated as an effective and noninvasive method with which to diagnose diseased tissue, especially early stage cancers.[1–12] Tissue autofluorescence is emitted from endogenous fluorophores excited by low-power, short-wavelength light. The autofluorescence measured on the tissue surface reveals some of the biochemical and biomorphological changes that are occurring in the tissue. Careful *in vivo* studies of several organ sites by calibrated fluorescence spectroscopy has shown that the tissue autofluorescence of early lesions is almost always less than that of the surrounding normal tissues, although the spectral line shapes of early lesions and normal tissues vary both from individual to individual and within an individual.[5,7,8] Tissue autofluorescence is not only a function of endogenous fluorophores but is affected by the tissue's optical properties as well, because tissue is a kind of turbid medium. Strong evidence indicates that a robust algorithm for discriminating a lesion from surrounding normal tissue should include information on the tissue's autofluorescence.

The calibrated fluorescence spectroscopy for *in vivo* study of tissue autofluorescence commonly utilizes a multiple optical fiber sensor to deliver the excitation light and collect the backscattered fluorescence signal.[5,7,8,12] The distal tip of the sensor is gently touched to the tissue surface to ensure constant fluorescence excitation-and-collection geometry for measurements at different sites. This point-by-point diagnosis method has been successfully used for detection of early cancers at various organ sites.[7,8] However, it is time consuming and not practical in clinical practice to examine a large area of tissue. It would be desirable to determine an imaging technique. For examination of a large area by an imaging device the recorded fluorescence is strongly affected by geometrical effects such as separation of the source–sample–detector, incident–emission angles, and irregularity of the sample surface. Without a mechanism to compensate for such geometrical effects, it is impossible to map the fluorescence in the imaged area, especially for *in vivo* measurements.

Several groups of researchers have studied geometrical effects on measurement of tissue fluorescence and explored various methods for determination of the relative fluorescence on tissue surfaces. Profio *et al.*[2] and Lenz[4] used a nonimaging approach to compensate

The authors are with the Department of Electrical and Electronic Engineering, Hong Kong University of Science and Technology, Clear Water Bay, Kowloon, Hong Kong, China. J. Y. Qu's e-mail address is eequ@ust.hk.

Received 7 June 1999; revised manuscript received 16 February 2000.

0003-6935/00/193344-13$15.00/0

for the inhomogeneity of fluorescence excitation and collection in tissue. In their studies the fluorescence signals were normalized to reflection signals of excitation light collected from the exactly same sites. The results showed that the geometrical effects could be corrected but that the artifacts caused by specular reflection from the tissue surface created many false positives. Analytical relations between fluorescence and diffuse reflectance have been developed,[13,14] based on photon migration and diffusion theories. It has been proved that, with knowledge of the tissue's optical properties, the diffuse reflectance at the wavelengths of fluorescence emission can be used to correct the distortion of the autofluorescence caused by the scattering and absorption of tissue. Further, Wu *et al*. stated that the ratio of fluorescence to effective reflectance at the same wavelength could correct the geometrical effects in fluorescence measurement.[13] Moreover, they pointed out that specular reflection from a tissue surface must be carefully avoided or subtracted in the clinical application of the ratio method. Assuming that the scattering properties vary little in different samples of the same tissue, they demonstrated that the ratio technique can be directly used to extract a tissue's intrinsic fluorescence and correct the geometrical effects. In the research reported in Ref. 9 the calibrated fluorescence spectral images were obtained from the tissue surface in a special geometry by use of a combined ultrasonic and fluorescence spectroscopic system. The technique may be invalid when the angular distribution of the backscattered ultrasonic signal is different from that of the fluorescence signal. Wang *et al*. reported an image-processing method for measurement of relative fluorescence on the tissue surface.[10] In a fully digital approach the raw fluorescence image of tissue is normalized to a reference image, which is a processed raw fluorescence image by use of the moving-average algorithm, a type of low-pass filter. To ensure that the lesions are filtered out and the excitation and collection nonuniformities are retained in the reference image, the algorithm requires that the lesion width be much smaller than the imaged area. The variation of fluorescence was assumed to be a slowly varying function over the tissue surface, because a low-pass spatial filter cannot distinguish a lesion from a geometrical artifact whose spatial frequency is distributed in the same region as the lesion.

In this paper we present a ratio imaging method that maps the relative fluorescence on the surface of a homogeneous turbid medium with optical properties in the range of human tissue. The technique utilizes the ratio of fluorescence (F) to diffuse reflectance (R) of the excitation light collected by a LIF imaging system to correct the geometrical effects in the fluorescence measurement. Our study was motivated by the well-established ratio technique reported in Ref. 13 and the research of Profio[2] and Lenz.[4] We analyze the technique by using the method of Monte Carlo modeling. The technique is then evaluated experimentally with a series of homogeneous and inhomogeneous tissue phantoms in various excitation-and-collection geometries. We demonstrate that the technique could image an early lesion based on the contrast in autofluorescence between the lesion and normal tissue. Finally, qualitative discussions on modeling and experimental results are presented.

2. Methods

For a conventional LIF imaging system the fluorescence and reflectance of excitation light are easily measurable. The reflected light from the turbid medium consists of three components: specular reflection, nearly diffusive backscattering (scattered 1–2 times), and diffusive backscattering (specular reflection does not carry any information about nonuniformity of illumination and collection). Wu *et al*. have proved that the analytical relationships between fluorescence and diffuse reflectance measured at the same wavelength can be used to correct geometrical effects in fluorescence measurement.[13] The question is whether one can use the diffuse reflectance of excitation light, one of the easily measured constituents of a LIF imaging system to correct geometrical effects in fluorescence measurement.

To find the answer to the question we first investigated the characteristics of fluorescence and diffuse reflectance of excitation light on a tissue surface. Instead of taking the approaches based on diffusion or photon migration theory, we chose the method of Monte Carlo modeling with which to calculate the tissue fluorescence and reflectance. Monte Carlo modeling does not assume that fluorescence and reflectance are diffusive waves, as do diffusion and photon migration theories. However, the major disadvantage of Monte Carlo modeling is that it is time consuming to generate data with a reasonably good signal-to-noise ratio (SNR). Briefly, one calculates the distribution of excitation light in tissue by convoluting that of an infinitely narrow beam and the profile of the illumination beam. One calculates the escape function of the endogenous fluorophore at various depths by treating the emission of fluorophores as an isotropic radiating point source inside the tissue. The product of the distribution of excitation and the fluorescence excitation efficiency yields the fluorescence source distribution in tissue. Finally, the fluorescence emerging from the tissue surface is obtained by convolution of the fluorescence source distribution and the fluorescence escape function. In general, the fluorescence collected from the tissue surface can be calculated by

$$\Psi_F(r, \lambda_{em}) = \int_0^\infty \Phi_F(r', z, \lambda_{ex}, \lambda_{em}) \otimes \Gamma_{escape}(r', z, \lambda_{em})dz, \quad (1)$$

$$\Phi_F(r, z, \lambda_{ex}, \lambda_{em}) = \Phi_{Ex}(r, z, \lambda_{ex}) \times \beta(r, z, \lambda_{em}), \quad (2)$$

$$\Phi_{ex}(r, z, \lambda_{ex}) = \Phi_{Ex}'(r', z, \lambda_{ex}) \otimes I_{profile}(r', \lambda_{ex}), \quad (3)$$

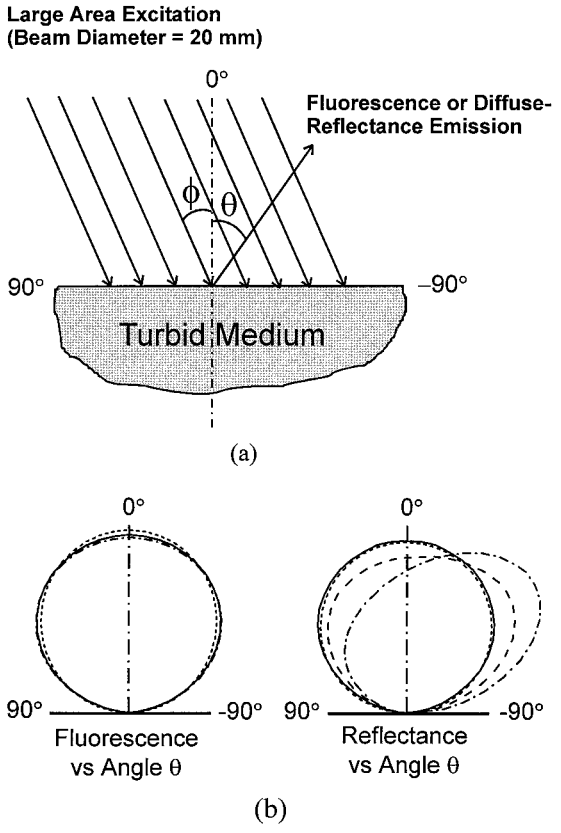

Fig. 1. Monte Carlo modeling of fluorescence and diffuse reflectance of excitation light. The optical properties of the tissue at the excitation wavelength are $\mu_a = 16.5\ \mathrm{cm}^{-1}$, $\mu_s = 184\ \mathrm{cm}^{-1}$, and $g = 0.9$ and at fluorescence wavelength are $\mu_a = 8.0\ \mathrm{cm}^{-1}$, $\mu_s = 145\ \mathrm{cm}^{-1}$, and $g = 0.87$. (a) Illumination-and-collection geometry: $\phi \in (0°, 90°)$ and $\theta \in (-90°, 90°)$. (b) Normalized angular distribution of fluorescence and diffuse reflectance emerging from the tissue surface. Solid circles, illumination angle $\phi = 0°$; long-dashed circle, $\phi = 30°$; dashed–dotted circles, $\phi = 75°$, short-dashed circles, Lambertian source.

where $\Phi_F(r, z, \lambda_{ex}, \lambda_{em})$ and $\Gamma_{escape}(r, z, \lambda_{em})$ are the fluorescence source distribution and fluorescence escape functions in the tissue, respectively. $\Phi_{Ex}(r, z, \lambda_{ex})$ and $\beta(r, z, \lambda_{em})$ in Eq. (2) are the distribution of excitation light and the fluorescence excitation efficiency at the emission wavelength, respectively. $\Phi_{Ex}'(r, z, \lambda_{ex})$ and $I_{profile}(r, \lambda_{ex})$ in Eq. (3) are the distribution of an infinitely narrow excitation beam and the true illumination beam profile, respectively. $\otimes$ refers to the convolution of two functions. A detailed description and discussion of Monte Carlo modeling for fluorescence and reflectance can be found in Refs. 8 and 15.

In the simulation, collimated uniform excitation (20 mm in diameter) and a semi-infinite tissuelike turbid medium with a flat surface were assumed. The illumination-and-collection geometry is shown in Fig. 1(a), in which θ and ϕ are the collection and illumination angles, respectively. We modified the Monte Carlo code of Wang and Jacques[15] to enable it to generate angularly and radially resolved fluorescence and reflectance at various illumination angles

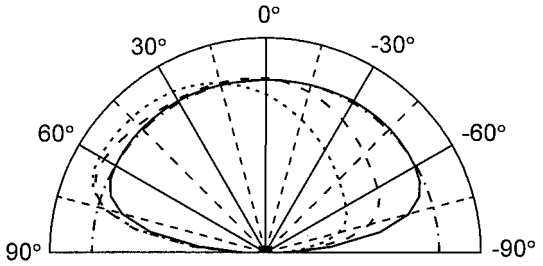

Fig. 2. Angular distribution of F/R ratio at several illumination angles ϕ in the incidence plane. Solid curve, $\phi = 0°$; long-dashed curve, $\phi = 30°$; short-dashed curve, $\phi = 75°$; dashed–dotted curve, reference.

(ϕ). A coefficient (μ_a), a scattering coefficient (μ_s), and an anisotropic factor (g) of the homogeneous sample were chosen to be in the range of typical human tissue.[16] 20×10^6 photons were launched for each simulation. We calculated the fluorescence and reflectance at illumination angles of 0° to 75° at intervals of 15°. The normalized distributions of calculated fluorescence and reflectance at three representative illumination angles are displayed in Fig. 1(b). For clear illustration and discussion, only the data in the incidence plane defined by the incidence axis and the normal of the tissue surface are displayed. It is not a surprise that the fluorescence is almost Lambertian, regardless of the illumination angle, because the fluorescence source is isotropic. The reflectance has a distribution that is nearly Lambertian when the illumination is perpendicular to the tissue surface ($\phi = 0°$). However, the symmetry of the reflectance is destroyed when the illumination becomes oblique. The major cause of the asymmetry is that tissue is the forward-scattering dominant turbid medium ($g \sim 0.9$, $\mu_s \gg \mu_a$). Backscattering with respect to the illumination axis is much less likely than forward scattering, which indicates that the diffusion and photon migration theories will produce errors in the calculation of angularly resolved reflectance because both theories treat fluorescence and reflectance as diffusive sources. Taking an approach similar to that of Profio[2] and Lenz,[4] we calculated the ratio (F/R) of fluorescence to reflectance of the excitation collected at the same angle (θ). The results are shown in Fig. 2. The dashed–dotted semicircle with a radius F/R angle $\theta = \phi = 0°$ is displayed as a reference. Comparing the F/R ratio in the various illumination-and-collection geometries with the reference, we can see clearly that, when angle θ is close to ϕ, the ratio value varies little and the F/R ratio effectively corrects the geometrical effect. In contrast, the fluorescence emission shown in Fig. 1(b) is highly dependent on collection angle θ as a Lambertian source. Our results are consistent with that stated by Wu *et al.*,[13] though the reflectance used in this F/R ratio method is at the wavelength of the excitation light instead of at that of the fluorescence emission. It should be emphasized that the correction by the F/R ratio method becomes invalid

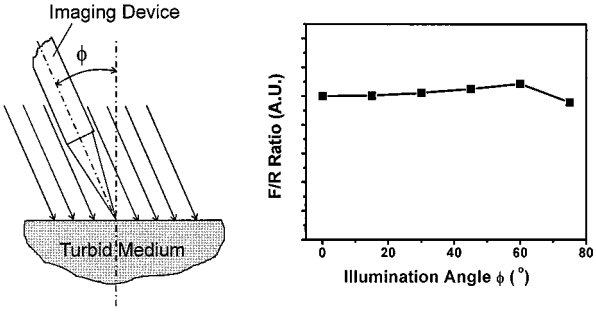

Fig. 3. F/R ratio collected by an imaging device such as an endoscope. Left, illumination-and-collection geometry; right, dependence of F/R ratio on illumination-and-collection angle.

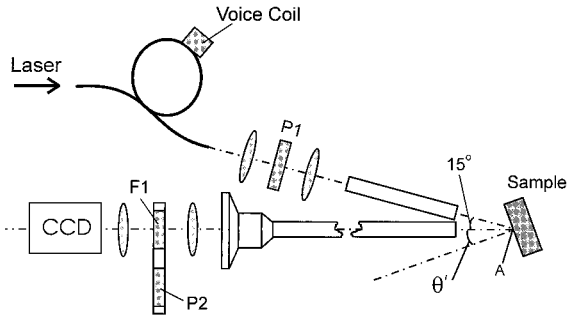

Fig. 4. Schematic diagram of the experimental setup used to collect the fluorescence and cross-polarized reflection images: F1, long-pass filter; P1, P2, polarizers with polarization axes perpendicular to each other; θ′, angle between the optical axis of the endoscope and the normal of the sample surface.

when F and R are collected at an angle far from the illumination axis, as we discuss in Section 5 below.

In a practical imaging system the fluorescence and reflectance signals are collected at a solid angle. We calculated the F/R ratio of a system that collects the signals within a cone of a $\pm 5°$ angle from the illumination axis. The collection geometry and results are shown in Fig. 3. As can be seen, the F/R ratio weakly depends on the illumination angle (ϕ). The correction of the geometrical effects is valid for a wide range of illumination angles.

It should be noted that the illumination-and-collection geometry in the model is not appropriate for many applications, such as endoscopic imaging systems. Also, the model was based on one set of optical properties of tissue. Nevertheless, the modeling results provide some insights into the relationship between fluorescence and excitation reflectance, and they seem encouraging. In principle, one can use Monte Carlo modeling to study this F/R ratio method in any fluorescence excitation-and-collection geometry. However, the computation time and data space will be significantly increased when a geometry with noncollimated illumination and an irregular tissue surface is modeled.[15] The experimental investigation is more efficient for studying the relation between fluorescence and reflectance in a practical geometry such as an endoscopic imaging system.

As we pointed out at the beginning of this section, the reflection of excitation light from a tissue surface includes three components. Although the diffuse reflectance may be used as the reference in the F/R ratio method to correct the geometrical effects, specular reflection will create artifacts.[2,4,13] Measures must be taken to remove specular reflection from the reflection of the excitation light and retain the diffusive components. Tissue is a kind of turbid medium. Light is scattered and absorbed during propagation inside the tissue. In the visible region the light in tissue is highly scattered and the transport of light is dominated by scattering events. It is well known that the polarization of light will be changed when a scattering event occurs. If the excitation light has a certain state of polarization, multiple scattering in the tissue, which yields diffusive reflectance, will randomize the state of polarization. In contrast, specular reflection maintains the original polarization state of the excitation light. Thus a polarization-sensitive imaging system can separate the specular and the diffusive reflectance components. Recently Demos and Alfano,[17] Demos *et al.*,[18] and Perelman *et al.*[19] used the polarization imaging techniques to characterize tissue structures.

To reject the specular reflection and extract the diffusive components from the total reflectance of excitation light we utilize a cross-polarization imaging method. Linearly polarized excitation was chosen for this study because linearly polarized light is more easily randomized than is circularly polarized light in a turbid medium.[20,21] Experimentally, we illuminate a tissue-simulating sample (turbid medium) with linearly polarized fluorescence excitation light and by the use of a polarization analyzer in front of the imaging sensor record the cross-polarized image. Because forward scattering dominates light propagation in the human tissue, the cross-polarized components in the reflection are produced mainly by multiple scattering and are highly diffusive. The information carried in the cross-polarization image comes predominantly from beneath the superficial layer.[17–19] The specular reflection and superficial information (mainly as a result of single backscattering) that cause artifacts in the correction of geometrical effects are almost completely removed in the cross-polarized image. Taking the ratio of the fluorescence signal to the cross-polarized reflection recorded from the same position forms a normalized fluorescence image. The geometrical effects can be corrected in the F/R ratio image by the approach reported in Ref. 13.

3. System and Materials

A. Experiment

The experimental arrangement for recording the cross-polarized and fluorescence images is shown in Figure 4. The excitation source was a solid-state frequency-doubled laser with output power of ~200 mW at a wavelength of 457 nm (blue microlaser, Laser Power Corporation). The laser light was de-

livered to the sample surface through an illumination optics consisting of a multimode optical fiber of 200-μm diameter, a linear polarizer, and microlenses of 1.6 mm-diameter. The fluorescence and reflection signals from the sample were collected by a standard commercial endoscope (7200A, Karl Storz) and imaged to an 8-bit CCD camera (WAT-502A, Watec, Inc.). The imaging channel of the endoscope was ~1.8 mm in diameter. The angle between the optical axes of the endoscope and the illumination optics was ~15°. The distal tips of the endoscope and the illumination optics were attached to each other and were located ~10 mm away from the surface of the sample. The imaged area on the sample surface, which was smaller than the illuminated area, was approximately 10 mm × 10 mm at $\theta = 0°$. To vary the geometry of illumination and collection, the sample could be rotated along the axis across point A and perpendicular to the plane of the page in Fig. 4. The holder of a long-pass filter with a cutoff wavelength at 470 nm and a polarizer with its polarization axis perpendicular to that of excitation light allows for easily selecting the fluorescence or the cross-polarized imaging channel. The system extinction ratio of the cross-polarized imaging channel is ~100:1. The extinction ratio is defined as the ratio of the maximal transmittance (parallel) for a linearly polarized light to the minimal transmittance (cross). The fluorescence and cross-polarized images are grabbed by a frame-grabber (Genesis-LC, Matrox Electronic Systems, Ltd.) at rate of 25 frames/s. To improve the signal-to-noise ratio we formed the fluorescence image by taking an average of 16 image frames. The ratio image of fluorescence versus cross-polarized reflection was then generated by a PC computer.

The SNR of the ratio image is strongly dependent on the quality of the fluorescence and the cross-polarized images. We found that the speckle effect did cause the quality of reflection image to deteriorate because the excitation was from a laser, a coherent source. Many methods to reduce the speckle effect and improve the image quality have been proposed.[22–24] Here we used a vibration mechanism reported in Ref. 22 to modulate the fiber and randomize the phases of the propagating modes in the fiber. In our experimental setup a small part of the fiber (~5 mm in length) was driven by a voice coil. When modulation was applied, the speckle pattern became a time-varying function that depended on the vibration amplitude and frequency. We found that the speckle noise in the reflection image can be effectively averaged out when the modulation frequency is set to ~600 Hz.

B. Tissue Phantoms

Tissue-simulating phantoms were made of gelatin that consisted of 20% solids dissolved in boiling deionized water, polystyrene spheres of 0.55-μm diameter (Polysciences, Inc.), a fluorescent dye mixture, and blood, the dominant absorber. The method for preparing the gel-based solid phantom has been well documented.[25,26] The scattering coefficients of the tissue phantoms, which were controlled by the concentration of polystyrene microspheres, were determined by two independent methods: measurements of the total attenuation coefficients and calculation by Mie theory.[27–31] In the first approach we measured the unscattered transmittance of an optically thin scattering sample that was made from the gel–microsphere mixture without adding any absorbers. The total attenuation coefficient, the scattering coefficient of a pure scattering sample, then could be obtained from the unscattered transmittance by the Beer–Lambert law. We used the spectrophotometer shown in Fig. 5 to determine the optical properties of the tissue phantoms. We used an optical fiber of 200-μm diameter to conduct broadband illumination from a white-light source (fiber optic illuminator 77501, Oriel). The light from the fiber was collimated into a beam of 2-mm diameter by the use of a lens and three apertures. The divergent angle of the beam was approximately 10 mrad. The transmission signal was collected by a lens–fiber system and analyzed by a spectrometer (MCS 55 UV-NIR, Zeiss). The thickness of the samples used in the measurements varied from 0.3 to 0.45 mm. In our calculation of scattering coefficient and anisotropic factor (g) by Mie theory we used the refractive indices of gel and polystyrene microspheres reported in Refs. 31 and 32. Figure 6(a) displays the experimentally measured and theoretically calculated scattering coefficients of the tissue phantoms used in this research. The experimental scattering coefficient of a microsphere concentration at 0.5% by weight (w/w) was extrapolated from the data at 0.25% and 0.35% w/w because the spectrometer was not sensitive enough to detect highly attenuated light. As can be seen, the experimental results are well consistent with the calculation of Mie theory. The calculated g factor is shown in Fig. 6(b). The scattering coefficients and anisotropic factor of the tissue phantoms were in the range of typical human tissue.[16]

The amount of absorption of tissue phantoms is determined by the concentration of blood, the dominant absorber. In this study, fresh blood was drawn from mice. Red cells were rinsed with phosphate-buffered saline (pH 7.4) and then lysed by addition of deionized water. Fragments of cell membranes were removed by centrifugation. The absorption co-

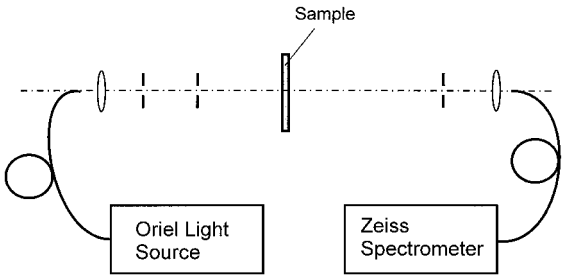

Fig. 5. Setup for measurement of the optical properties of the samples.

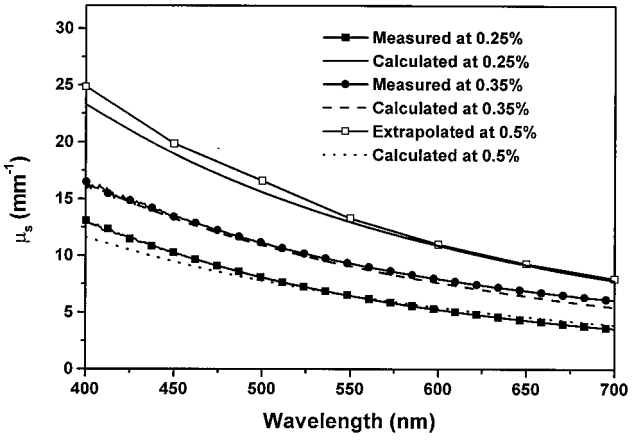

(a)

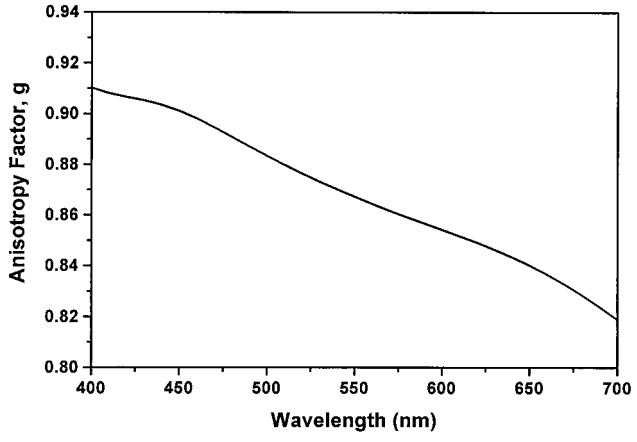

(b)

Fig. 6. Scattering coefficients and g factors of tissue-simulating phantoms used in the study. (a) Measured and calculated scattering coefficients at concentrations of polystyrene microsphere in the tissue phantom of 0.25%, 0.35%, and 0.5% w/w. (b) Calculated g factors of 0.55-μm-diameter polystyrene microspheres in the gel.

efficient of the hemolyzed blood was measured with the spectrophotometer shown in Fig. 5. The concentration of hemoglobin (most cells were oxygenated) could be determined by the ratio of measured absorption coefficient to that of pure oxyhemoglobin reported in Refs. 33 and 34. By controlling precisely the hemoglobin concentration in the gel, we set the content of blood with a hematocrit of 0.51 for the three groups of tissue phantoms that we used to 2.5%, 5%, and 7.5% by volume (v/v).

To simulate fluorophores in the tissue we used a mixture of highly efficient green and red Stabilo Boss dye fluorescent highlighters. A typical fluorescence spectrum of a tissue phantom measured by a spectrometer is shown in Fig. 7. The fluorescence spectral coverage of the dye mixture is also in the range of *in vivo* measured autofluorescence of human tissues.[1–12] The absorption of the fluorescence dyes at the concentration used in the tissue phantoms is much less than that of blood and can be negligible.

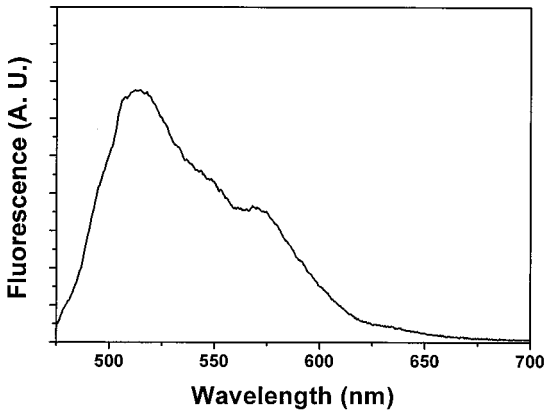

Fig. 7. Fluorescence spectrum of a tissue phantom excited by a laser of 457-nm wavelength.

All samples used in this study were ~25 mm in diameter and 4.5 mm thick.

4. Results

A. Homogeneous Phantoms

We demonstrate that the geometrical effects on fluorescence imaging of the homogeneous tissue phantom can be corrected to a great extent by the F/R ratio imaging method. In the first experiment, all the samples with different optical properties were homogeneous and had flat surfaces. The compositions of the samples are listed in Table 1. We changed the imaging geometry by rotating the sample along the axis across point A and perpendicular to the plane of the page in Fig. 8. The fluorescence and cross-polarized images were collected from all tissue phantoms at $\theta' = 0°–60°$ in increments of 15°. For the measurements at large angles θ, the illumination became highly nonuniform. We did not perform a measurement for $\theta' > 60°$ because of the limited dynamic range and sensitivity of our 8-bit CCD camera. Also, the image blurring caused by aberrations in the imaging system became the major source of error as angle θ became greater than 60°.

For a fair comparison, the mean gray levels of all the raw fluorescence images and ratio images of fluorescence against cross-polarized reflection were adjusted to 128, half of the full gray levels of an 8-bit image. The typical raw fluorescence and ratio images are shown in Fig. 9. The histogram for the gray level in the figure indicate the homogeneity of the

Table 1. Composition of Homogeneous Phantoms with Flat Surfaces

Sample Number	Blood Content (v/v, %)	Concentration of Polystyrene Microsphere (w/w, %)
1	2.5	0.25
2	5.0	0.25
3	7.5	0.25
4	2.5	0.5
5	5.0	0.5
6	7.5	0.5

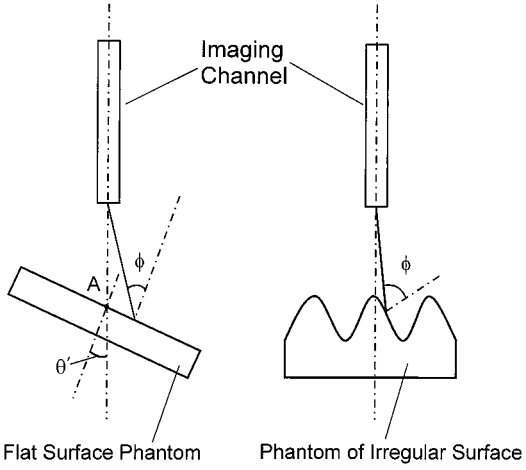

Fig. 8. Simplified geometry of the experimental imaging system. Left, Imaging of a flat surface phantom at $\theta' \neq 0$; right, imaging of a phantom with an irregular surface at $\theta' = 0°$. ϕ is the excitation-and-collection angle.

image. As can be seen from Fig. 9, the raw fluorescence image is highly nonuniform and the gray levels vary across a wide range. In contrast, the ratio image is uniform and its gray level has a narrow distribution about 128, the mean gray level. We found that the standard deviations of gray levels for the raw fluorescence images recorded from all six phantoms varied from 24 to 41 at $\theta' = 0°–60°$, whereas the standard deviations of the ratio images fell into a range from 1.8 to 4.5, much smaller than that for the raw fluorescence images.

In the second experiment we examined the performance of the ratio technique for imaging of a homogeneous sample with an irregular surface. The profile of the phantom surface was constructed as shown in Fig. 8. The width and the depth of the grooves were ~8 mm and ~5 mm, respectively. The blood content and the concentration of polystyrene microsphere of the phantom used in the experiment were 5% v/v and 0.35% w/w, respectively. The fluorescence and cross-polarization images were taken in the same fashion as for the first experiment at $\theta' =$

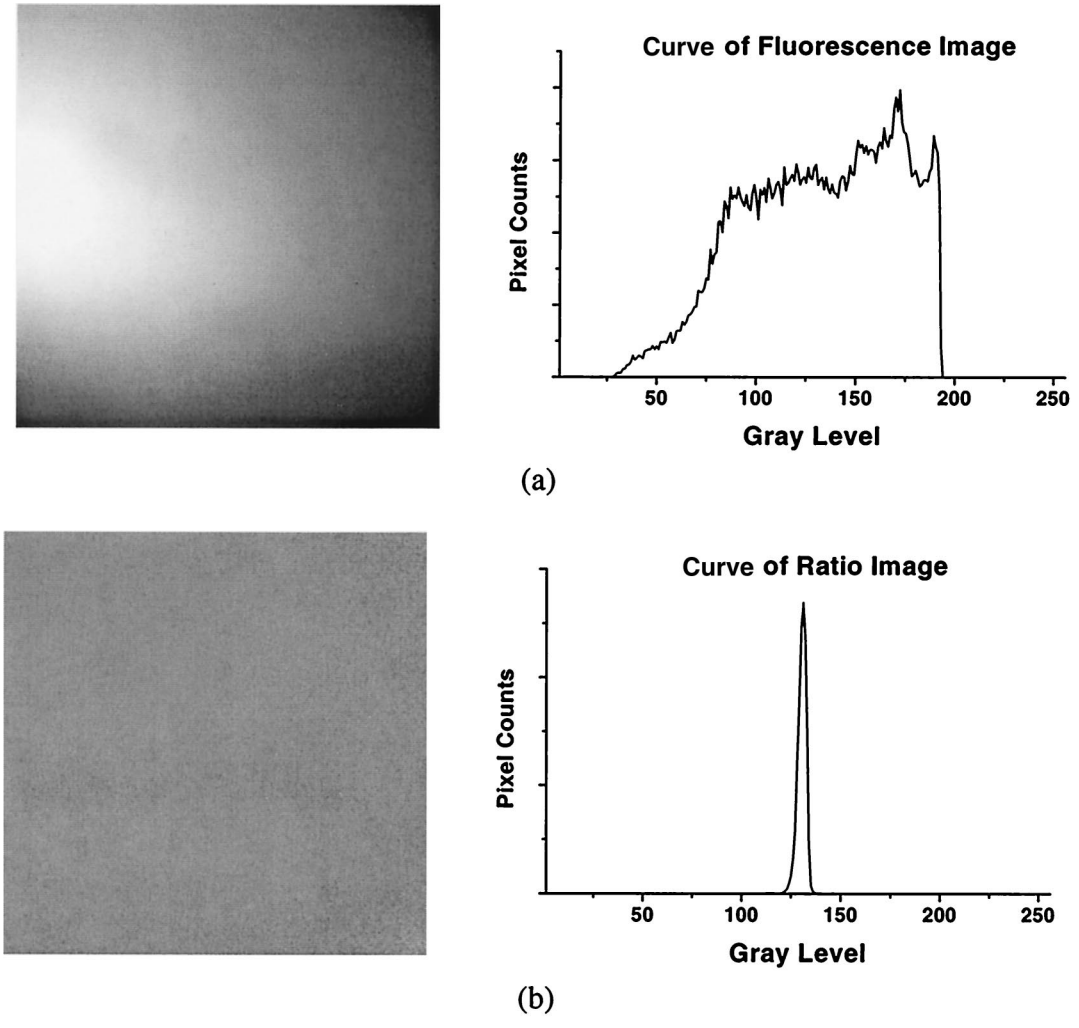

Fig. 9. Images collected from a tissue-simulating phantom with a blood content of 2.5% (v/v) and a microsphere concentration of 0.5% (w/w) at $\theta' = 30°$. (a) Raw fluorescence image and histogram of its gray level, (b) F/R ratio image and its histogram.

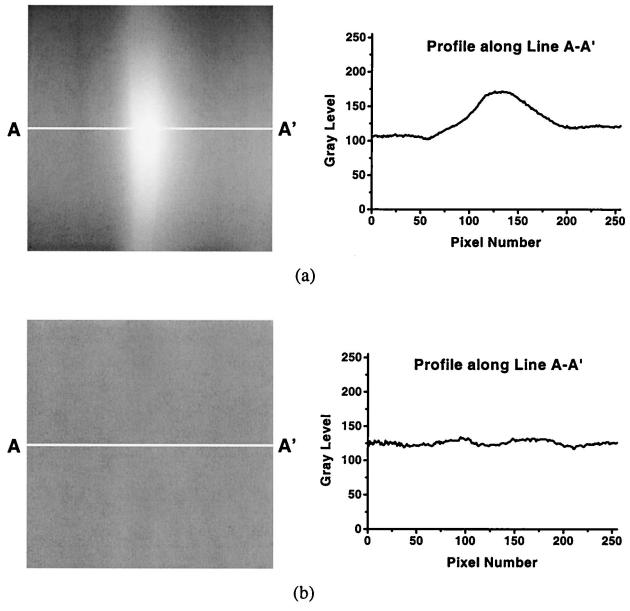

Fig. 10. Raw fluorescence image and ratio image recorded from the homogeneous phantom of an irregular surface. (a) Raw fluorescence and the profile across A–A', (b) ratio image of fluorescence versus cross-polarized reflection and profile across A–A'. The standard deviations of the gray levels of the raw fluorescence and ratio images are 32 and 5, respectively.

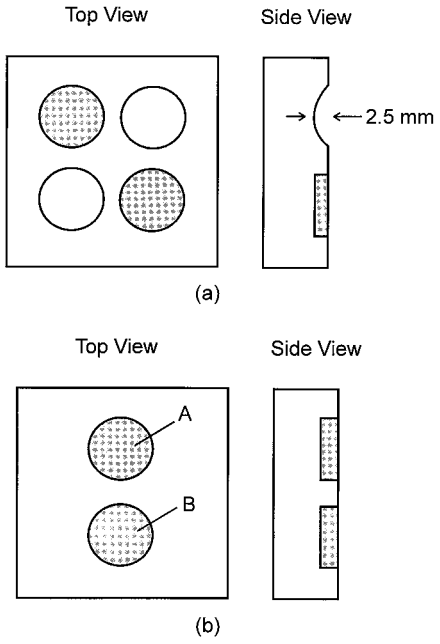

Fig. 11. Structures of inhomogeneous tissue-simulating phantoms: (a) fluorescence yield contrast phantom, (b) absorption and scattering contrast phantoms.

0°. The raw fluorescence and ratio images are shown in Fig. 10. As can be seen, the inhomogeneity in the raw fluorescence has been significantly compensated for by the F/R ratio imaging technique.

B. Inhomogeneous Phantoms

In this study we evaluated the performance of the F/R ratio imaging on inhomogeneous tissue phantoms. We classified the phantoms based on the amount of inhomogeneity in the concentration of fluorophores and optical properties. To construct an inhomogeneous tissue phantom we replaced parts of the homogeneous sample with samples of different fluorophore concentrations or optical properties. For the fluorescence contrast phantom shown in Fig. 11(a) the parts of the homogeneous sample in the shaded areas were replaced with simulated lesions of slightly lower fluorescent dye concentration and the same optical properties. The blood content and the microsphere concentration of the phantom were set to 5% and 0.35%, respectively. Two shallow holes were made to make the surface irregular and to create geometrical interference for identifying the simulated lesions. The structure of the absorption and scattering contrast phantoms is shown in Fig. 11(b). For the absorption contrast phantom the parts of the sample in areas A and B were replaced with samples of 10% and 2.5% blood content, respectively. The blood content of the surrounding sample was 5%. The concentration of polystyrene microspheres in all samples that we used to construct the absorption contrast phantom was set to 0.35%. For the scattering contrast phantom, samples in areas A and B were replaced with samples of microsphere concentrations 0.5% and 0.35%, respectively. The microsphere concentration of the surrounding sample was 0.25%. The blood content in all samples for the construction of the scattering contrast phantom was set to 5%. The concentrations of fluorescent dyes in all the absorption and scattering contrast phantoms were constant.

The results shown in Fig. 12 are the raw fluorescence and ratio images of three inhomogeneous phantoms. The back-to-back comparison of the raw fluorescence and ratio images demonstrates again that the geometrical effects have been well corrected in the F/R ratio method. The image of the fluorescence yield contrast phantom demonstrates that the ratio technique can clearly identify the simulated lesions that yield slightly lower fluorescence. In the raw fluorescence image, one cannot separate the artifacts created by two holes from the simulated lesions. However, only the simulated lesions that yield low fluorescence appear clearly in the ratio image, and the geometrical artifacts caused by the holes were almost completely eliminated. Furthermore, the ratio image of the absorption contrast phantom shows that the variation of fluorescence signal caused by the uneven distribution of blood has been compensated for effectively. The results from the measurement of the scattering contrast phantom suggest that the variation of scattering property across the tissue surface can be detected in the F/R ratio image.

5. Discussion

We found that specular reflection in the cross-polarized image was significantly reduced by a cross-polarization imaging system with an extinction ratio

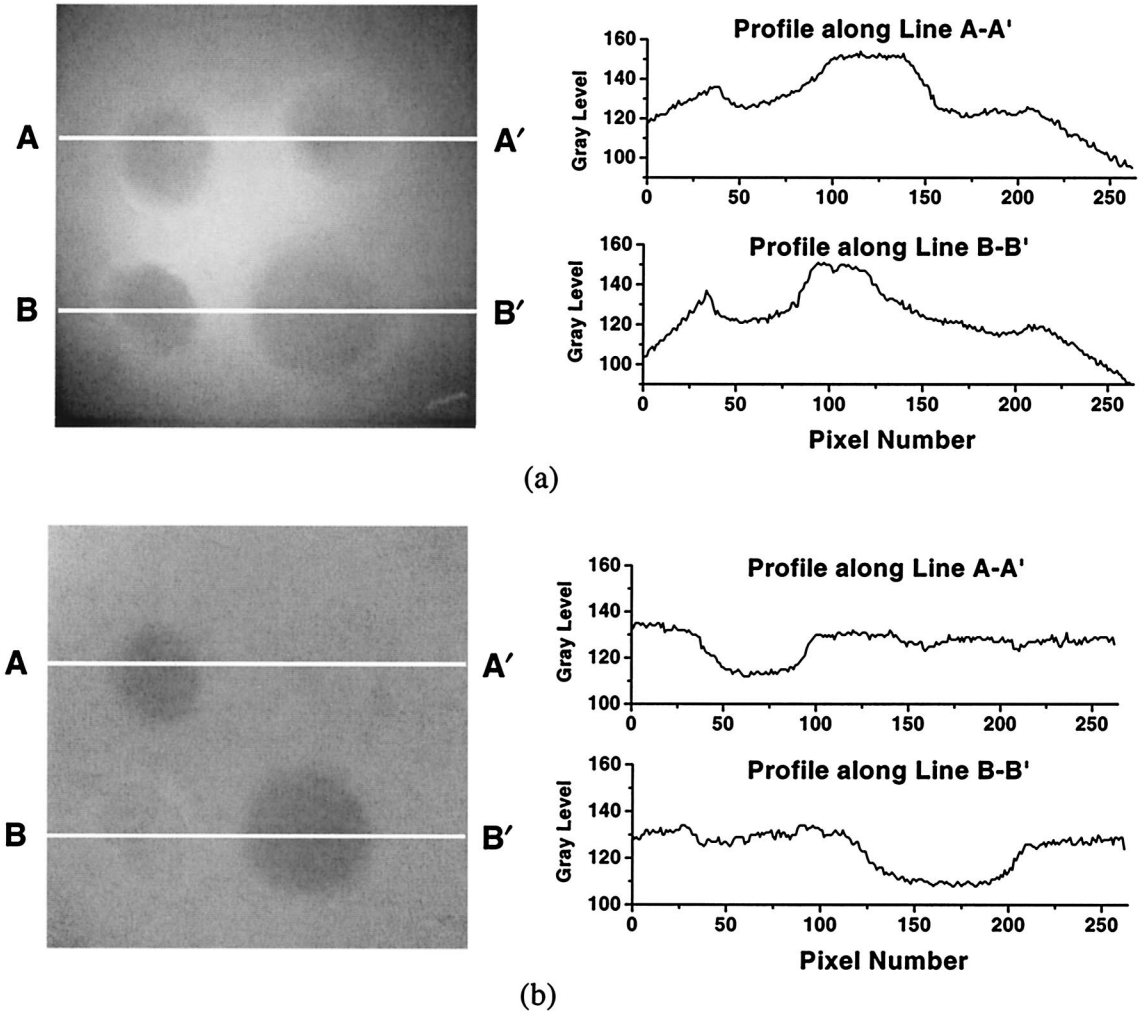

Fig. 12. Results of imaging of inhomogeneous phantoms. (a) and (b) Raw fluorescence and ratio images taken from a fluorescence yield contrast phantom. Figure 12 continues on the next page.

of 100:1. The image shown in Fig. 13(a) is a reflection image taken from the fluorescence yield contrast phantom at $\theta' = 0°$ with the polarizer in the cross-polarization imaging channel removed. The specular reflection signal in the image is much higher than that of diffusive reflection and a saturated large area of CCD sensor. Comparing the F/R images in Fig. 13 with that in Fig. 12(b) makes clear that specular reflection causes major artifacts if the direct reflection signal is used as the reference to compensate for the geometrical effects in the F/R ratio technique. We could further improve the performance of the system used in this study by optimizing the optical design and increasing the extinction ratio.

In the measurements of the homogeneous phantom with a flat surface, the homogeneity of the ratio image decreased slightly as angle θ' increased but was not sensitive to the polarization plane of the excitation light and to the optical properties of samples. In the measurements of the homogeneous phantom with an irregular surface, the line profile analyses in Fig. 10 show that a small variation of the pixel value in the ratio image does have a weak correlation with the profile of the sample surface. These results indicate that the excitation incident angle and the fluorescence collection angle play roles, though insignificant ones, in determining the F/R ratio value obtained. The simplified geometry of our imaging system is shown in Fig. 8. The excitation incident angle and the fluorescence collection angle are assumed to be the same because the sizes of the illumination microlens and the endoscope lens are much smaller than the distance from the sample to the distal tips of the endoscope and the illumination optics. The range of excitation-and-collection angle ϕ for a phantom with a flat or irregular surface is then determined by the degree of irregularity in the surface and by angle θ'. In Fig. 14 we display the pixel value of ratio images as a function of angle ϕ based on measurements of all homogeneous tissue phantoms. The value of the ratio increases slightly as ϕ increases in the range 0–70°. This result seems consistent with the results of Monte Carlo modeling shown in Fig. 3, although the experimental and modeling geometries for endoscopic imaging are different. The ratios at angle $\phi > 70°$ were not measured for the

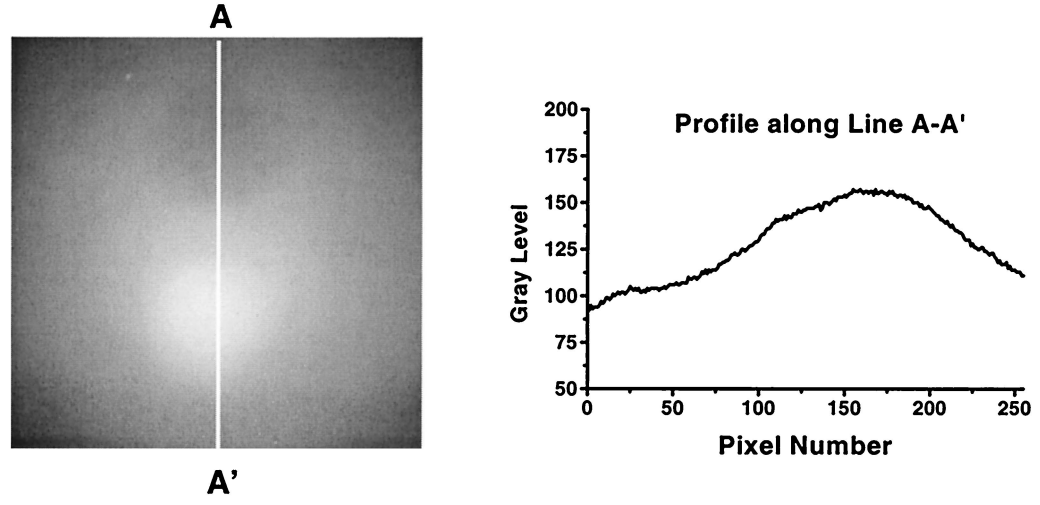

(c)

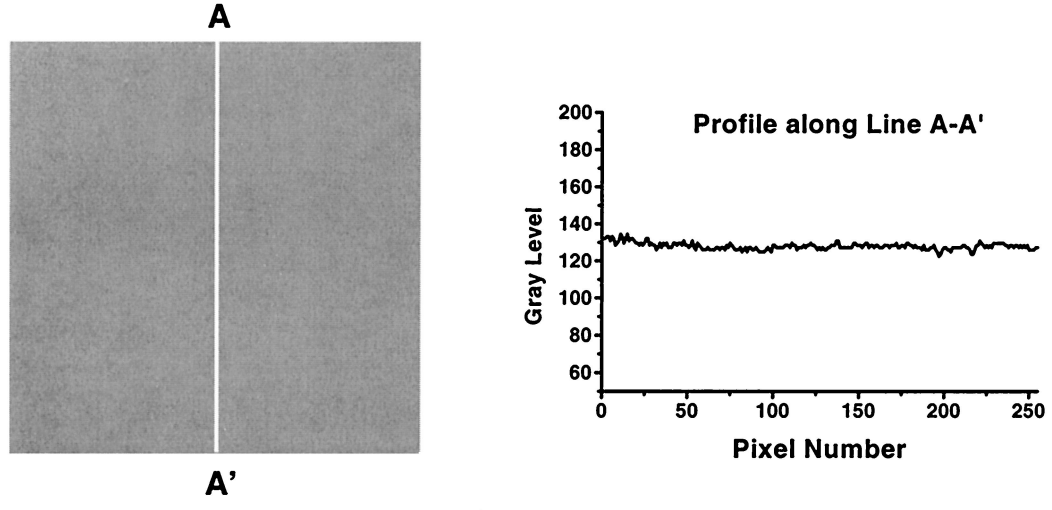

(d)

Fig. 12. (c) and (d). Raw fluorescence and ratio images of the absorption contrast phantom. Figure 12 continues on the next page.

reasons discussed in Section 3. We found that the maximal variation of ratio in the range of angle ϕ from 0 to 70° is less than 7%. This sets the accuracy or sensitivity in relative fluorescence mapping of tissuelike turbid media.

The results of Monte Carlo modeling in Fig. 2 show that the F/R ratio remains constant and that the geometrical correction is valid for F and R collected in a specific range of backscattering angle (calculated as $|\phi - \theta|$) from the illumination axis. Angles θ and ϕ are defined in Fig. 1(a). However, the ratio value drops quickly when backscattering angle $|\phi - \theta|$ becomes large. This shows that the reflectance has a similar angular distribution to the fluorescence for a small backscattering angle from the illumination axis but not for a large angle. The difference is caused mainly by the contribution of the nearly diffusive component that is the result of photons scattered once or twice in the tissue[35] to the total diffuse reflectance, which consists of both a nearly diffusive component and a diffusive component. The diffusive component is produced by multiple scattering and has characteristics similar to those of Lambertian fluorescence. As light propagation in tissuelike turbid media is dominated by forward scattering ($g \sim 0.9$), the probability of a single-scattering event in a small backscattering angle is much smaller than for a large backscattering angle and forward scattering. Thus the nearly diffusive reflectance must be dominated by photons backscattered in a large angle ($|\phi - \theta|$) from the illumination axis. In contrast, small-angle backscattering from tissue is dominant in diffusive reflectance, which has an angular distribution similar to that of Lambertian fluorescence. The contribution of the nearly diffusive component to the total diffuse reflectance becomes significant with increasing backscattering angle $|\phi - \theta|$. Therefore the nearly diffusive photons in the total reflectance cause a decrease in the F/R ratio and invalidate the geometrical correction in a large backscattering angle

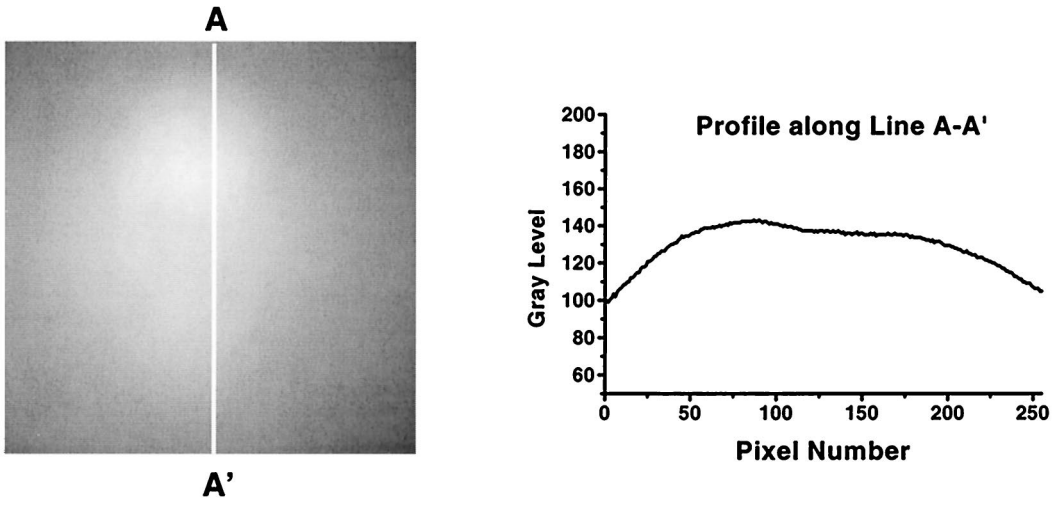

(e)

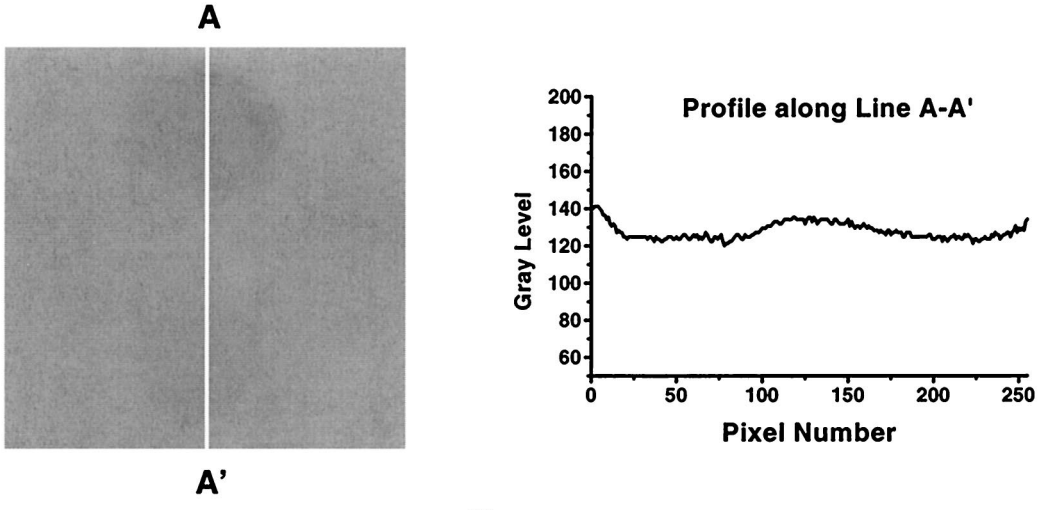

(f)

Fig. 12. (e) and (f) Raw fluorescence and ratio images of the scattering contrast phantom.

$|\phi - \theta|$. For good correction of the geometrical effect the fluorescence and the diffuse reflectance must be collected in a small backscattering angle in which the contribution of the diffusive component to the total diffuse reflectance is dominant. Apparently, the endoscopic imaging system used in the experimental study satisfies that condition.

The measurement of the fluorescence contrast phantom demonstrates that the ratio imaging method can identify simulated lesions that have a fluorescence that is slightly lower than that of the surrounding sample and can eliminate geometrical artifacts. Quantitatively, the fluorescence of the simulated lesions used in the experiment was set to ~80% of that of the surrounding samples. In raw fluorescence it was not possible to distinguish the lesions from the artifacts created by two shallow holes on the surface of the sample. In the ratio image the difference in fluorescence between simulated lesions and simulated normal tissue was obvious. Line profile analysis has shown that the border between the simulated lesions and the simulated normal tissue is smooth because of the migration of fluorescence photons from the surrounding samples

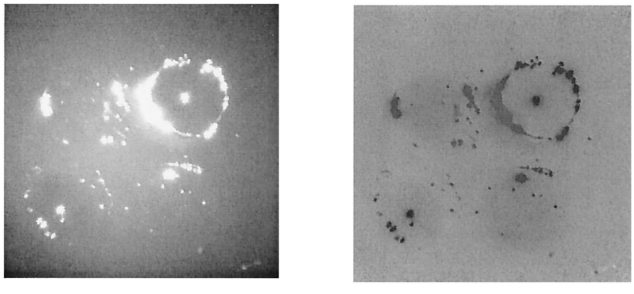

Fig. 13. Left, reflection image recorded without the cross polarizer; right, F/R ratio image without the cross polarizer.

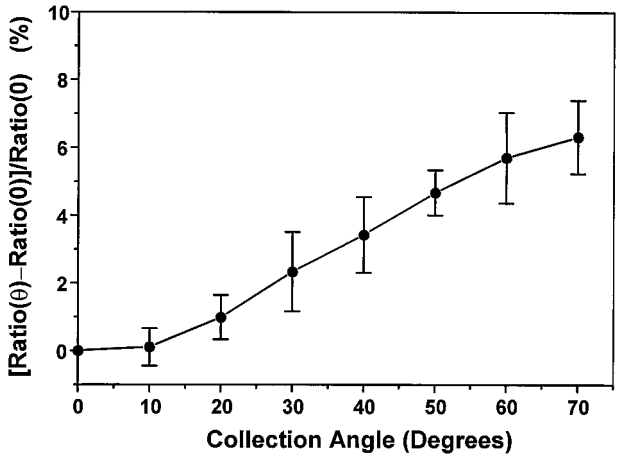

Fig. 14. Relative change of F/R ratio as a function of excitation and collection angle θ. The vertical axis is the difference between the ratio at angle θ and at 0° divided by the ratio at 0°.

to the simulated lesion areas. A clinical study showed that the contrasts in fluorescence between early lesions and normal tissue in many organ sites are greater than in our phantom.[5–8,10] Our results hold the promise for potential application to identifying early lesions clinically by the use of the ratio imaging technique.

It is an important finding that the ratio method can effectively correct the artifacts caused by variation of blood content in the sample. The blood in tissue is usually not evenly distributed, depending on local vascularization. As a dominant absorber, blood strongly affects the distribution of excitation light in tissue. The fluorescence intensity of tissue is correlated to local blood content, as shown in the raw fluorescence image recorded from the absorption contrast phantom. A variation of blood content also appears in the cross-polarized reflection image. However, the F/R ratio image indicates that the effects of absorption on fluorescence and diffuse reflectance signals can cancel each other. In the measurement of the scattering contrast phantom we found that the reflectance is affected by variation of the scattering coefficient, whereas the fluorescence signal is less sensitive to changes in scattering. It appears that the uneven distribution of scatterers does not significantly contribute to the inhomogeneity of a raw fluorescence image. The geometrical effects are corrected in the ratio image, but the high and low scattering areas appear clearly and create artifacts in maps of fluorescence yield. Fortunately, the structure of real tissue, which determines the scattering coefficients, is not likely to vary so suddenly as in the scattering contrast phantom. The artifacts of scattering may not play an important role in clinical applications.

6. Conclusions

A combination of cross-polarized and fluorescence imaging techniques has been successfully used to correct geometrical effects in fluorescence measurement of tissuelike turbid media. This technique permits mapping of fluorescence yield over a homogeneous tissue surface. The sensitivity and accuracy of the detection of variations in fluorescence depend weakly on the excitation incident and fluorescence collection angles. Based on the experimental results, the ratio imaging technique can identify a variation of fluorescence in tissue of greater than 7% when excitation incident and fluorescence collection angles are in the range 0–70°. It should be emphasized that the theoretical analysis and the experimental study were done with single-layered tissuelike samples. As was discussed in Ref. 13, real tissues are usually multiply layered; their fluorophores are distributed as a function of depth. Extensive *in vivo* investigation will be needed to evaluate the performance of this ratio technique for clinical practice. Our future research will focus on understanding the relation between polarized light and fluorescence in tissue and on constructing an endoscopic imaging system based on the ratio method for *in vivo* study of autofluorescence of human tissue.

This research was funded by Hong Kong Research Grants Council grants CA97/98.EG01 and HKUST6207/98P and by the Hong Kong University of Science and Technology.

References

1. R. R. Alfano, D. B. Tat, J. Cordero, P. Tomashefsky, F. W. Longo, and M. A. Alfano, "Laser induced fluorescence spectroscopy from native cancerous and normal tissue," IEEE J. Quantum Electron. **QE-20,** 1507–1511 (1984).
2. A. E. Profio, D. R. Doiron, and J. Sarnaik, "Fluorometer for endoscopic diagnosis of tumors," Med. Phys. **11,** 516–520 (1984).
3. C. Kittrell, P. L. Willett, C. de los Santos-Pacheo, N. B. Ratliff, J. R. Kramer, E. G. Malk, and M. S. Feld, "Diagnosis of fibrous arterial atherosclerosis using fluorescence," Appl. Opt. **24,** 2280–2281 (1985).
4. P. Lenz, "Endoscopic fluorescence detector," Rev. Sci. Instrum. **59,** 930–933 (1988).
5. R. M. Cothren, R. R. Richards-Kortum, M. V. Sivak, M. Fitzmaurice, R. P. Rava, G. A. Boyce, G. B. Hayes, M. Doxtader, R. Blackman, T. Ivanc, M. S. Feld, and R. E. Petras, "Gastrointestinal tissue diagnosis by laser-induced fluorescence spectroscopy at endoscopy," Gastrointest. Endosc. **36,** 105–111 (1990).
6. J. Hung, S. Lam, J. C. LeRiche, and B. Palcic, "Autofluorescence of normal and malignant bronchial tissue," Lasers Surg. Med. **11,** 99–105 (1991).
7. N. Ramanujam, M. F. Mitchell, A. Mahadevan, S. Thomsen, E. Silva, and R. Richards-Kortum, "Fluorescence spectroscopy: a diagnostic tool for cervical intraepithelial neoplasia (CIN)," Gynecol. Oncol. **52,** 31–38 (1994).
8. J. Qu, C. MacAulay, S. Lam, and B. Palcic, "Laser-induced fluorescence spectroscopy at endoscopy: tissue optics, Monte Carlo modeling, and *in vivo* measurements," Opt. Eng. **34,** 3334–3343 (1995).
9. S. Warren, K. Pope, Y. Yazdi, A. J. Welch, S. Thomsen, A. L. Johnston, M. J. Davis, and R. Richards-Kortum, "Combined ultrasound and fluorescence spectroscopy for physico-chemical imaging of atherosclerosis," IEEE Trans. Biomed. Eng. **42,** 121–132 (1995).
10. T. D. Wang, J. van Dam, J. M. Crawford, E. A. Preisinger, Y. Wang, and M. S. Feld, "Fluorescence endoscopic imaging of

human colonic adenomas," Gastroenterology **111,** 1182–1191 (1996).
11. G. A. Wagnieres, A. P. Studzinski, and H. E. van den Bergh, "An endoscopic fluorescence imaging system for simultaneous visual examination and photodetection of cancers," Rev. Sci. Instrum. **68,** 203–212 (1997).
12. K. Tumer, N. Ramanujam, J. Ghosh, and R. Richards-Kortum, "Ensembles of radial basis function networks for spectroscopic detection of cervical precancer," IEEE Trans. Biomed. Eng. **45,** 953–961 (1998).
13. J. Wu, M. S. Feld, and R. P. Rava, "Analytical model for extracting intrinsic fluorescence in turbid media," Appl. Opt. **32,** 3585–3595 (1993).
14. C. M. Gardner, S. L. Jacques, and A. J. Welch, "Fluorescence spectroscopy of tissue: recovery of intrinsic fluorescence from measured fluorescence," Appl. Opt. **35,** 1780–1792 (1996).
15. L. Wang and S. L. Jacques, "Monte Carlo modeling of light transport in multilayered tissue in standard C" (University of Texas, Houston, Tex., 1992).
16. W. F. Cheong, S. A. Prahl, and A. J. Welch, "A review of the optical properties of biological tissues," IEEE J. Quantum Electron. **26,** 2166–2185 (1990).
17. S. G. Demos and R. R. Alfano, "Optical polarization imaging," Appl. Opt. **36,** 150–155 (1997).
18. S. G. Demos, A. J. Papadopoulos, H. Savage, A. S. Heerdt, S. Schantz, and R. R. Alfano, "Polarization filter for biomedical tissue optical imaging," Photochem. Photobiol. **66,** 821–825 (1997).
19. L. T. Perelman, V. Backman, J. Wu, R. R. Dasari, and M. S. Feld, "Spectroscopic diagnostics of epithelial tissues with polarized light," in *Optical Tomography and Spectroscopy of Tissue III*, B. Chance, R. R. Alfano, and B. J. Tromberg, eds., Proc. SPIE **3597,** 474–479 (1999).
20. J. M. Schmitt, A. H. Gandjbakhche, and R. F. Bonner, "Use of polarized light to discriminate short-path photons in a multiply scattering medium," Appl. Opt. **31,** 6535–6546 (1992).
21. G. D. Lewis, D. L. Jordan, and P. J. Roberts, "Backscattering target detection in a turbid medium by polarization discrimination," Appl. Opt. **38,** 3937–3944 (1999).
22. S. Jutamulia and T. Asakura, "Reduction of coherent noise using various artificial incoherent sources," Optik **70,** 52–57 (1985).
23. R. Smith, S. Ahmad, A. Voudas, J. Spencer, A. Russel, and G. R. Jones, "Chromatic modulation for optical fiber sensing electromagnetic and speckle noise analysis," J. Mod. Opt. **39,** 2301–2314 (1992).
24. T. Iwai and T. Asakura, "Speckle reduction in coherent information processing," Proc. IEEE **84,** 765–781 (1996).
25. B. W. Pogue, L. Lilge, M. S. Patterson, B. C. Wilson, and T. Hasan, "Absorbed photodynamic dose from pulsed versus continuous wave light examined with tissue-simulating dosimeters," Appl. Opt. **36,** 7257–7269 (1997).
26. L. Wang and X. Zhao, "Ultrasound-modulated optical tomography of absorbing objects buried in dense tissue-simulating turbid media," Appl. Opt. **36,** 7277–7282 (1997).
27. S. L. Jacques, C. A. Alter, and S. A. Prahl, "Angular dependence of HeNe laser light scattering by human dermis," Lasers Life Sci. **1,** 309–333 (1987).
28. W. Pickering, S. A. Prahl, N. van Wierington, J. F. Beek, H. J. C. M. Sterenborg, and M. J. C. van Gemert, "Double-integrating-sphere system for measuring the optical properties of tissue," Appl. Opt. **32,** 399–410 (1993).
29. J. Qu, C. MacAulay, S. Lam, and B. Palcic, "Optical properties of normal and carcinomatous bronchial tissue," Appl. Opt. **33,** 7397–7405 (1994).
30. A. J. Drukin, S. Jaikumar, and R. Richards-Kortum, "Optically dilute, absorbing, and turbid phantoms for fluorescence spectroscopy of homogeneous and inhomogeneous samples," Appl. Spectrosc. **47,** 2114–2121 (1993).
31. M. Kohl, M. Essenpreis, and M. Cope, "The influence of glucose upon the transport of light in tissue-simulating phantoms," Phys. Med. Biol. **40,** 1267–1287 (1995).
32. D. W. Leonard and K. M. Meek, "Refractive indices of the collagen fibrils and extrafibrillar material of the corneal stroma," Biophys. J. **72,** 1382–1387 (1997).
33. E. J. van Kampen and W. G. Zilstra, "Determination of hemoglobin and its derivatives," in *Advances in Clinical Chemistry*, H. Sobotka and C. P. Stewart, eds. (Academic, New York, 1965), Vol. 8, pp 158–187.
34. O. W. van Assendelft, *Spectrophotometry of haemoglobin derivatives* (Royal Vangorcum, Assen, The Netherlands, 1970).
35. L. Wang and S. L. Jacques, "Analysis of diffusion theory and similarity relations," in *Photon Migration and Imaging in Random Media and Tissues*, B. Chance and R. R. Alfano, eds., Proc. SPIE **1888,** 107–116 (1993).